

A new graph-based surrogate model for rapid prediction of crashworthiness performance of vehicle panel components

Haoran Li ¹, Yingxue Zhao ¹, Haosu Zhou ¹, Tobias Pfaff ², Nan Li ^{1*}

¹ Dyson School of Design Engineering, Imperial College London, London, UK

² Google DeepMind, London, UK

* Corresponding author. E-mail address: n.li09@imperial.ac.uk (N. Li)

Abstract

During the design cycle of safety critical vehicle components such as B-pillars, crashworthiness performance is a key metric for passenger protection assessment in vehicle accidents. Traditional finite element simulations for crashworthiness analysis involve complex modelling, leading to an increased computational demand. Although a few machine learning-based surrogate models have been developed for rapid predictions for crashworthiness analysis, they exhibit limitations in detailed representation of complex 3D components. Graph Neural Networks (GNNs) have emerged as a promising solution for processing data with complex structures. However, existing GNN models often lack sufficient accuracy and computational efficiency to meet industrial demands. This paper proposes Recurrent Graph U-Net (ReGUNet), a new graph-based surrogate model for crashworthiness analysis of vehicle panel components. ReGUNet adopts a U-Net architecture with multiple graph downsampling and upsampling layers, which improves the model's computational efficiency and accuracy; the introduction of recurrence enhances the accuracy and stability of temporal predictions over multiple time steps. ReGUNet is evaluated through a case study of side crash testing of a B-pillar component with variation in geometric design. The trained model demonstrates great accuracy in predicting the dynamic behaviour of previously unseen component designs within a relative error of 0.74% for the maximum B-pillar intrusion. Compared to the baseline models, ReGUNet can reduce the averaged mean prediction error of the component's deformation by more than 51% with significant improvement in computational efficiency. Provided enhanced accuracy and efficiency, ReGUNet shows greater potential in accurate predictions of large and complex graphs compared to existing models.

Keywords: Artificial intelligence; Deep learning; Surrogate modelling; Graph neural network; Crashworthiness analysis

1 Introduction

Vehicle lightweighting has been one of the most focused topics in the automotive industry due to the growing concern about global climate change [1]. Companies and researchers are dedicating significant efforts to exploring innovative design methodologies for vehicle components aimed at realising the lightweighting objective while maintaining high performance. For vehicle safety critical components like the A-pillar, B-pillar, and front roof cross member, crashworthiness performance is the most crucial factor to be considered during structural design. This measures the component's ability to protect passengers in potential vehicle accidents, including deformation resistance and energy absorption during collision. Typical crashworthiness analysis of a vehicle component involves studying the dynamic behaviour of the component during crash tests. For example, side impact crash tests evaluate the vehicle's behaviour in lateral collisions, where the B-pillar is one of the most focused components during the tests [2]. Common crashworthiness indicators include maximum B-pillar intrusion and energy absorption.

While vehicle crash tests provide reliable insight into component crashworthiness performance, they are too expensive to be used iteratively in design cycles. Therefore, finite element (FE) simulations are extensively used in the prediction of component crashworthiness performance. High-fidelity FE simulations, however, may require significant computational resources for complex scenarios. For example, crash test simulations involve large metal deformations under high strain rates, resulting in highly nonlinear calculations. Moreover, the process of design optimisation of automotive components often demands iterative trial-and-error approaches. This can be notably time-consuming with FE simulations due to the aforementioned limitations.

Machine learning (ML)-based surrogate modelling has emerged as a promising solution to the aforementioned limitation. The surrogate models are usually constructed using artificial neural networks (ANNs), which aim to approximate complex simulations with a reduction of computational resource consumption. The application of ANN-based surrogate models has shown potential within the area of crashworthiness. Most existing surrogate models [3-8] were based on multilayer perceptron (MLP) and were designed for the prediction of scalar quantities such as the crashworthiness indicators. A few studies [9, 10] used recurrent neural networks (RNNs) for time series data predictions, which are essential for crashworthiness analysis. In time series data, numerous measurements, such as acceleration profiles and force-time histories, are recorded over specific time intervals. Both MLP and RNN-based models are restricted to predictions based on scalar inputs and outputs, they exhibit limitations in fully describing the detailed behaviours of complex simulations, such as collision modes. To overcome this limitation, field-based models developed using convolutional neural networks (CNNs) have been proposed to predict high-fidelity physical fields, such as displacement fields during impact [11, 12]. Field-based models enable more comprehensive and detailed analyses of component behaviours during impact. However, CNN-based surrogate models are limited to Euclidean data structures, such as images. They have limited capabilities of processing complex geometries characterised by non-Euclidean data structures, such as irregular meshes. This limitation highlights the importance of the development of more advanced surrogate models that can process more complex data structures while maintaining a high level of accuracy.

Graph neural networks (GNNs) are particularly designed for graphs, which are based on non-Euclidean data structures, making it a promising solution to the aforementioned limitation. A graph consists of a set of nodes, with edges connecting nodes that are related to each other. This structure naturally makes them a suitable representation form for complex irregular FE meshes containing mesh nodes and elements. GNNs are the neural networks operating on graph data, achieving various types of tasks like node-level regression or classification. Recent studies have utilised GNNs in mechanics-related domains such as continuum solid mechanics [13-16], computational fluid dynamics [17-20], and metamaterial modelling [21, 22]. Specifically, GNNs have been employed to perform node regression tasks for Lagrangian mesh-based simulations [23-25]. These existing models have demonstrated efficacy in relatively simple case studies, such as small graphs evaluated under basic conditions such as quasistatic loading. Their performance on real-world case scenarios with more complex loading conditions and larger and more complicated graph structures remains less explored. These studies

established a strong foundation for GNN applications in mechanics-related domains at industrial-level contexts that address practical challenges. To the best of the authors' knowledge, the application of GNNs in crashworthiness analysis is still in its early stages. A review of the existing GNN applications in crashworthiness analysis and similar fields is presented in Section 2.

In this paper, we propose a new GNN-based surrogate model, named Recurrent Graph U-Net (ReGUNet), for predicting vehicle panel components' dynamic behaviours under impact. The model has a U-Net architecture inspired by the CNN U-Net [26], which consists of downsampling and upsampling layers with skip connections. As a result, the model is capable of performing efficient spatial message passing within large graphs with several thousands of nodes. The model operates in a recurrent manner, propagating hidden state between time steps, making it especially suitable for temporal data prediction. The proposed model is evaluated using a B-pillar crash test case study. The model is trained on FE simulations of a side impact test on the B-pillar component with various geometric designs. This paper first reviews relevant existing GNN applications in similar fields of study in Section 2. This is followed by introducing ReGUNet, including explaining the graph representation methods and the neural network architecture in Section 3. After that, the case study used to evaluate ReGUNet is described in Section 4. The evaluation of the performance of ReGUNet is discussed in Section 5. This is followed by concluding the current work and stating the future directions in Section 6.

2 Related work

The use of GNNs in crashworthiness analysis is still in its very early stages. Wen et al. [27] proposed a model combining GNN with Temporal Convolutional Neural Networks (TCN) for predicting the nonlinear response of irregular vehicle components. A component can be represented in terms of graph data, consisting of nodes and edges. Each node represents a discrete segment of the space domain, and the edges define the adjacency of the segment. The construction of graph sequence enables the representation of not only the geometrical information of the component but also the time-based characteristics. This can be concluded as the spatiotemporal dynamics of the structure. While the nodes and edges determine the geometry of the component, the node features contain information on measurements of crashworthiness analysis. In the case study, crashworthiness indicators like the specific energy absorption and crash force were incorporated as node features within the graph sequence. The constructed graph sequence is input into an encoder-decoder architecture together with global input parameters such as initial velocity of impact. The architecture encodes the graph sequence into latent features by a number of spatiotemporal GNN layers, where each layer consists of two gated temporal convolutional layers [28] for temporal modelling, followed by a graph convolutional network [29] capturing spatial information. The correlations between the input parameters and the spatiotemporal dynamics are captured during the training process.

GNN models have been employed in the simulation of other dynamic systems in several studies. For instance, Deshpande et al. [13] proposed the Multi-channel Aggregation Network (MAgNET) for the prediction of non-linear mesh-based simulations. Mesh data is defined in terms of graph, where each graph node represents a mesh node, and each graph edge represents a mesh edge. The MAgNET consists of Multi-channel Aggregation (MAg) layers which assign a non-shareable weight to each edge of the graph for local feature aggregation. Unlike conventional CNNs using shareable weights (sliding kernels), the non-shareable weight matrix allows more accurate non-linear feature prediction across different channels.

Sanchez-Gonzalez et al. [30] developed the Graph Network-based Simulators (GNS) for predicting the motions of physical systems with particles. GNS follows an encoder-processor-decoder architecture. The framework is based on a sequence of Graph Network (GN) blocks to achieve long range message passing across graph data. GNS has been evaluated by making predictions of the motions of water, solid objects, and sand particles. Pfaff et al. [23] adopted and improved this framework by proposing the MeshGraphNet (MGN). MGN was specifically designed for mesh-based data prediction utilising message passing neural network [31]. The model introduces extra world-edges in addition to the mesh-edges to achieve message passing across different graphs to better simulate collisions. To perform node-level prediction task, the model uses MLPs as edge and node update functions.

Stacking a sequence of GN blocks allows message passing for multiple steps. However, this results in a significant increase in GPU memory consumption when processing large graphs. To address this limitation, Fortunato et al. [25] proposed the MultiScale MeshGraphNet (MS-MGN). The MS-MGN has a hierarchical architecture, which performs message passing across graphs with different resolutions. Higher efficiency is achieved due to the reduced number of message passing steps required from one global location to another in the low-resolution graph compared to the high-resolution graph. Information is propagated between graphs through downsampling and upsampling layers. Graphs with different resolutions are constructed based on manually produced meshes. Cao et al. [24] proposed an alternative downsampling approach with their Bi-Stride Multi-Scale GNN (BSMS-GNN). In this study, a novel bi-stride downsampling technique was introduced based on the breadth-first search (BFS), without having to manually construct meshes for low-resolution graphs. The graph size can be reduced by striding and pooling all nodes at every other BFS frontier. There are other graph downsampling approaches such as the spatial proximity approach [32-34], Guillard’s coarsening algorithm [35], and the clustering-based pooling method [13]. All these different approaches serve the same purpose of reducing the complexity of graph data, hence improving model’s efficiency. One limitation of these automated graph downsampling approaches is the potential loss of uniformity in the downsampled graphs, which may adversely impact the accuracy of message-passing operations.

Common GNN tasks in mechanics often involve temporal data prediction, where the objective is to predict feature evolution over time. For example, Pfaff et al. [23] used MGN to predict mesh deformation of metal plates under quasistatic loading. The deformation is divided into certain time intervals and each training iteration predicts the incremental deformation during each time interval. The prediction of the next immediate step is based on the previous steps, resulting in an increase in rollout error when the number of time steps increases. Chen et al. [16] proposed the physics-informed edge recurrent simulator (Piers) to improve this limitation. Piers was developed based on MGN, with the incorporation of RNN and physics-informed factors. In the GNN cell, the edge update function is replaced with a gated recurrent unit (GRU) layer, which is a special RNN layer with a reset gate and an update gate to better capture long-range dependencies. This results in a reduction in rollout error when the number of time steps increases and leads to a more stable prediction.

Most of the aforementioned GNN models have been evaluated on relatively simple case studies. In the solid mechanics field, MGN and its extended models are capable of predicting plate deformation under quasistatic loading conditions. High-speed dynamic systems are often more complex as they become highly nonlinear. Piers was designed for the prediction of dynamic responses of continuous deformable bodies (CDBs) with nonlinearity. However, the graph size is limited as the GPU memory consumption would be substantial with large graphs. For crashworthiness analysis of vehicle panel components, high-speed impact and fine mesh configuration are inevitable. Surrogate model training typically involves hundreds of samples with varying geometric designs, therefore, model efficiency becomes a crucial factor to consider when designing the architecture. In this paper, we propose the Recurrent Graph U-Net (ReGUNet), which is specifically tailored to overcome the aforementioned limitations.

3 The development of the new graph-based surrogate model

This section presents a detailed description of the Recurrent Graph U-Net (ReGUNet). We first introduce the graph representation form of FE meshes, followed by an explanation of the model architecture. The model aims to predict the impact dynamics of panel components given varying geometry designs, with a series of B-pillar designs employed as a case study. The data used for training is generated using FE simulations of the side impact test for the B-pillars.

3.1 Graph representation of FE meshes

A typical graph G can be expressed by $G = (\mathbf{u}, V, E)$, where \mathbf{u} is the global graph feature, $V = \{v_1, v_2, \dots, v_n, \dots, v_N\}$ is a set of nodes and $E = \{e_1, e_2, \dots, e_m, \dots, e_M\}$ is a set of edges connecting nodes. N and M are the numbers of nodes and edges, respectively. The connectivity of a graph describes how the nodes are connected by edges, which can be represented by the edge index. An edge index matrix E_{index} is a $2 \times M$ matrix containing the node indices connected by each edge, and can be represented as

$$E_{index} = \begin{bmatrix} v_{s_1} & v_{s_2} & \dots & v_{s_M} \\ v_{r_1} & v_{r_2} & \dots & v_{r_M} \end{bmatrix}, \quad (1)$$

where v_s and v_r are the sender and receiver nodes of each edge, respectively. On this graph, data can be stored by locally embedding it in the node feature vector $\mathbf{x}_{v_n} \in \mathbb{R}^{p_v}$ and the edge feature vector $\mathbf{x}_{e_m} \in \mathbb{R}^{p_e}$, where p_v and p_e are the dimensions of the node and edge feature vectors, respectively. The assembled matrices $\mathbf{X}_V \in \mathbb{R}^{N \times p_v}$ and $\mathbf{X}_E \in \mathbb{R}^{M \times p_e}$ denote the node and edge feature matrices, respectively. In a deep GNN, multiple layers are typically employed. The features are aggregated and propagated through each layer, where $\mathbf{X}^{(l)}$ and $\mathbf{x}^{(l)}$ denote the hidden node or edge feature matrix and vector at the l -th layer.

The graph data representation of the FE mesh of a B-pillar is illustrated in Figure 1. Similar to the existing methods [16, 23, 25], each graph node represents an FE mesh node, and edges connect any pairs of nodes that belong to the same mesh element. In order to predict the impact dynamics of the component, the crash simulation is divided into equally spaced time intervals. The temporal evolution of crash dynamics is thus described by a sequence of graphs $G_{seq} = [G^{t_1}, G^{t_2}, \dots, G^{t_T}]$, where T is the total number of time steps. As no mesh refinement is applied to the simulations, the graph connectivity stays constant throughout all time steps. The node and edge features, which represent the physics-field information of interest and change dynamically with time, describe the current state of the graph.

We encode graph features as follows: The node feature vector of each node consists of 3 components, $\mathbf{x}_{v_n}^{t_i} = (s_{n_x}^{t_i}, s_{n_y}^{t_i}, s_{n_z}^{t_i})$, where s denotes the incremental displacements in the x, y, and z directions for node v_n during the time interval t_i . In order to achieve a translation-invariance, we do not encode any absolute shape information into nodes. Rather, we encode the relative distances between nodes into edge features. For an edge e_m , the edge feature vector at time t_i consists of 8 components, $\mathbf{x}_{e_m}^{t_i} = (d_{m_x}^{t_i}, d_{m_y}^{t_i}, d_{m_z}^{t_i}, |d_m^{t_i}|, d_{m_x}^{t_0}, d_{m_y}^{t_0}, d_{m_z}^{t_0}, |d_m^{t_0}|)$, where d denotes the relative distances in the x, y, and z directions, and $|d|$ denotes the Euclidean distance between the two nodes. The edge feature vector includes information at both time t_i and time t_0 . This information describes both the component's current shape during impact and its original shape. Taking the input node and edge features, the model predicts an updated set of node features $\mathbf{x}_{v_n}^{t_{i+1}}$, namely the incremental displacements for each node at time interval t_{i+1} .

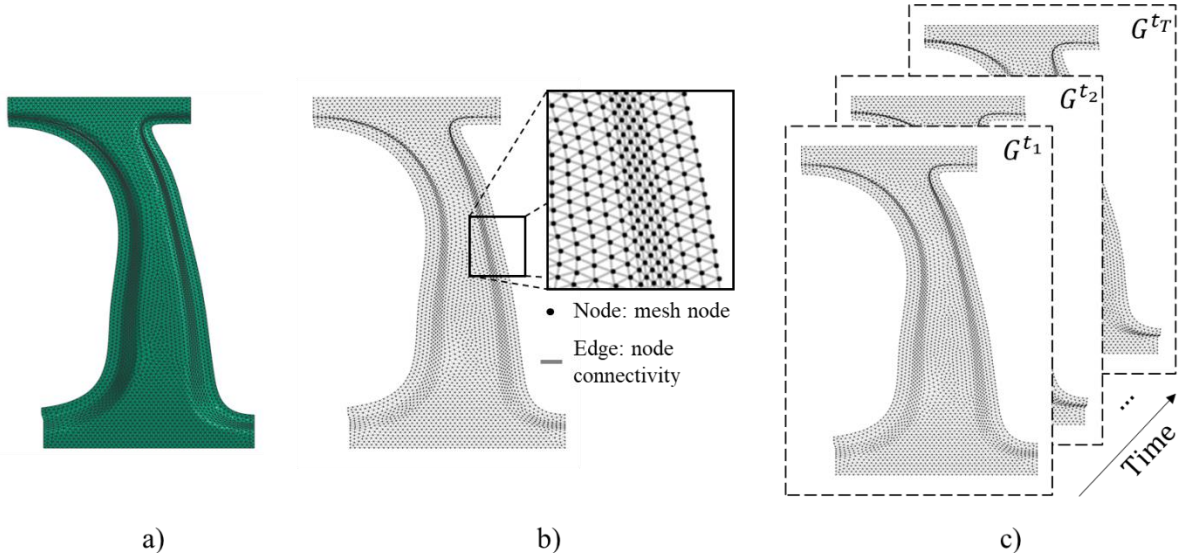


Figure 1: Illustrations of data representation for a B-pillar. a) FE mesh data of the B-pillar b) Graph representation of the B-pillar at a single time step c) The whole graph sequence consisting of T graphs over time.

3.2 Multi-scale graph representation

One iteration of message passing propagates information from each node to its immediate neighbouring nodes. Solid mechanics simulations however often involve long-range dynamics due to stiff material,

in which nodes can affect each other even if they are not in close proximity. Worse, crash simulations of vehicle components often require fine mesh configurations. This means that in order to propagate information over the graph, hundreds of iterations of message passing may be required. In order to reduce computational burden and improve model efficiency, multi-scale message passing is used, similar to MS-MGN[25]. Here, messages are being passed both on the fine-scale graph for local feature capturing, as well as on multiple levels of coarsened graphs, for faster information propagation. This message passing strategy is explained in detail in Section 3.3.

To solve solid mechanics-related problems, the coarsened graphs need to preserve the overall component structure and maintain the relative uniformity of the mesh. Therefore, coarsened graphs are created using FE meshes with larger element sizes. Figure 2 demonstrates the graph coarsening process of the B-pillar model. During each level of graph coarsening, the element size increases by a factor of 2, leading to a reduction of total number of nodes by a factor of 4. After 3 iterations of coarsening, the number of nodes reduces from around 3500 to 90, while preserving the overall shape and relatively uniform node distribution.

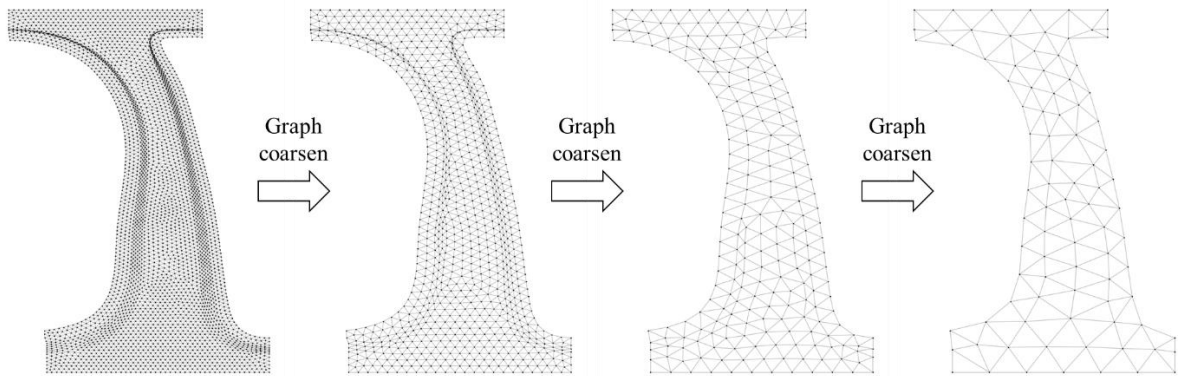


Figure 2: Demonstration of graph coarsening of the B-pillar component.

The coarsened graphs are generated from a benchmark sample, which has the initial geometrical design. This is the benchmark sample used for dataset generation via mesh morphing, which will be explained in more detail in Section 4. As a result, the fine graphs from all samples are downsampled to the same set of coarsened graphs. This approach is chosen for two reasons: firstly, in component design optimisation tasks, despite the variation in design features across samples, all samples exhibit a similar overall structure; secondly, this ensures a fixed number of edges in the coarsened layers, which significantly improves both accuracy and efficiency during cross-graph message passing. This will be further explained in Section 3.3.4

We use a graph U-Net architecture, with multiple layers of downsampling and upsampling. For passing information between graphs of different levels, edges are connected between the fine and coarse graphs. Figure 3 illustrates the edge connection between two different layers. The core concept is that for each node from the fine layer, find k nodes in the coarse layer that are the spatially closest to it and connect them. Figure 3 shows an example of cross-graph edge connection of 1 node when $k = 3$. This method ensures that all nodes from the fine layer are connected to those in the coarse layer to avoid any potential loss of information during downsampling and upsampling.

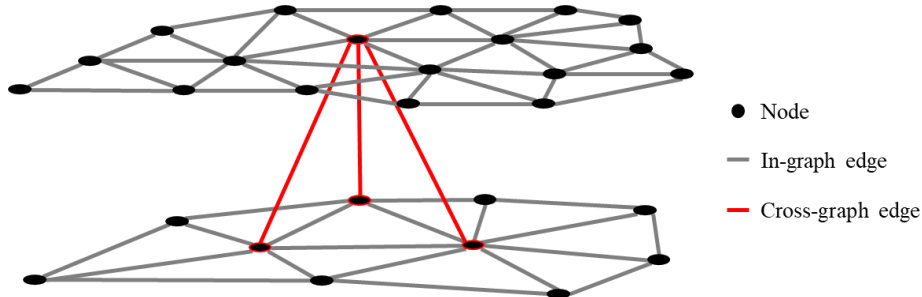


Figure 3: Illustration of the cross-graph edge connection for graph downsampling and upsampling processes.

3.3 Recurrent Graph U-Net

In this section, the architecture of ReGUNet is detailed explained. An overview of the architecture is first provided, followed by details of each component of the model.

3.3.1 The overall architecture of ReGUNet

ReGUNet is designed for predictions of temporal graphs with time sequence structure. Previous studies [11, 16] have demonstrated the performance improvements achieved by recurrent architectures in temporal prediction tasks, therefore, adopting the idea, ReGUNet operates in a recurrent manner. Figure 4 a) illustrates the overall architecture of ReGUNet when predicting a graph sequence with T time steps. The core of the model is the GUNet block, which performs prediction of the next time step based on the input from the current time step and the hidden state. An initial hidden state is input in the first iteration of prediction together with the first graph from the sequence. For each time step, the GUNet receives the hidden state from the previous time step \mathbf{H}^{t_i} . It then outputs the updated hidden state $\mathbf{H}^{t_{i+1}}$, which is directly fed into the next iteration, as well as the node features for the next-step input. Note that the overall hidden state \mathbf{H} includes two sets of hidden state matrices \mathbf{H}_f and \mathbf{H}_c , for the fine and coarse levels respectively. $T - 1$ rounds of node feature predictions are made until the final time step is reached.

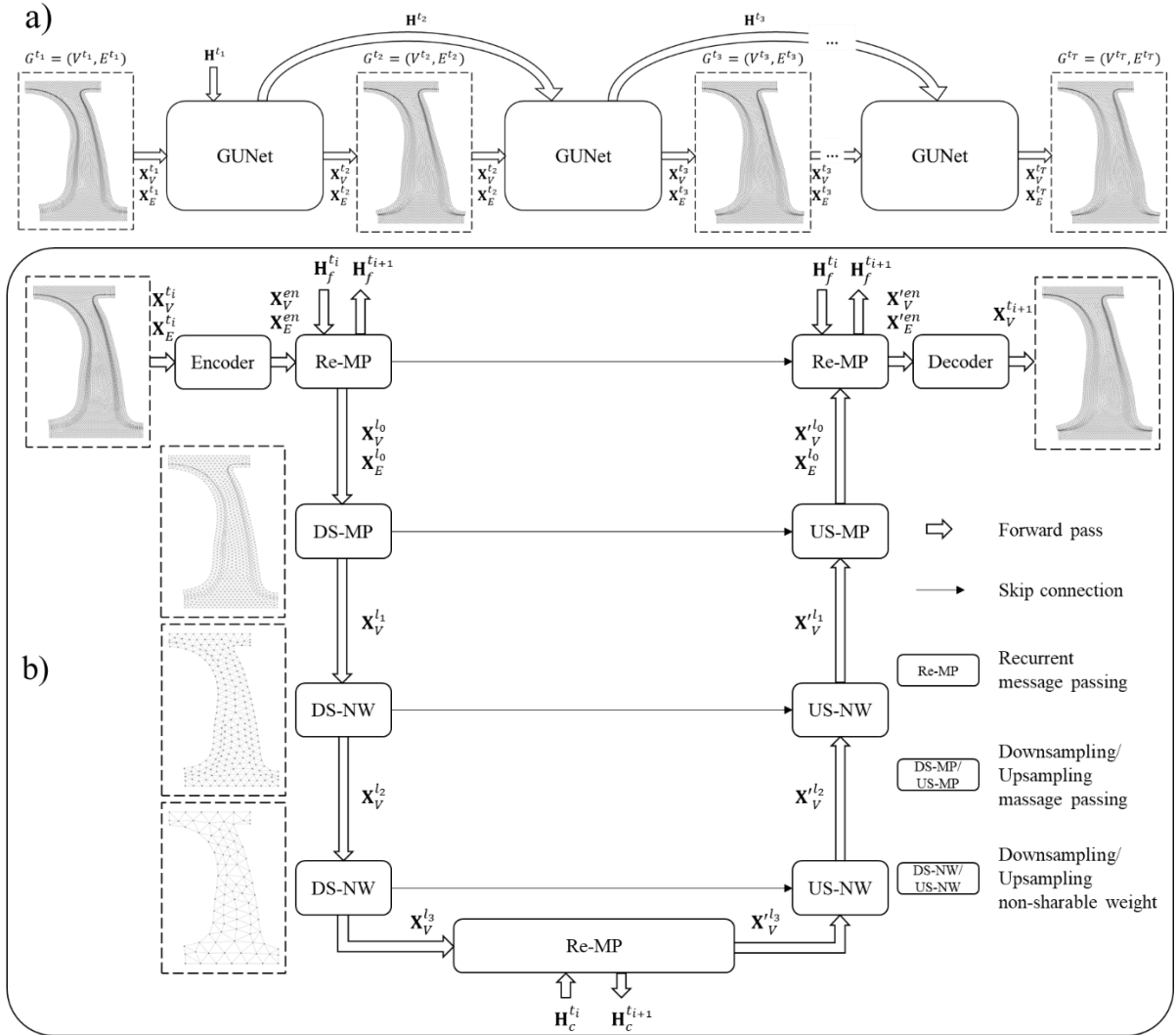


Figure 4: Illustrations of a) the overall recurrent architecture for prediction of a graph sequence, b) the architecture of the individual GUNet block from t_i to t_{i+1} .

Figure 4 b) illustrates the internal architecture within a GUNet block. At time step t_i , the input graph with node and edge feature matrices $\mathbf{X}_V^{t_i}$ and $\mathbf{X}_E^{t_i}$ first goes through an encoder which encodes the input

features to the latent space, denoted as \mathbf{X}_V^{en} and \mathbf{X}_E^{en} . Together with the fine-layer-hidden-state $\mathbf{H}_f^{t_i}$ from the previous time step, the encoded features are then updated with a recurrent message passing (Re-MP) layer with P_f message passing steps. The Re-MP layer returns the updated features for layer l_0 , $\mathbf{X}_V^{l_0}$ and $\mathbf{X}_E^{l_0}$, as well as the hidden state $\mathbf{H}_f^{t_{i+1}}$ which is directly fed into the next time step. This is followed by a number of downsampling layers propagating information to the most coarsened graph. The number of downsampling layers depends on the mesh density of the FE simulation data. Normally, a denser mesh requires more levels of graph downsampling to achieve efficient long-range message passing at the coarsest layer. In the example shown in Figure 4, three downsampling layers, including one message passing downsampling layer (DS-MP) and two non-shareable weight downsampling layers (DS-NW), are used. Note that edge features are not considered for the non-shareable weight layers as common coarsened graphs are used. For the Re-MP at the coarsest level, although in-graph edge feature matrix is used for message passing, it remains unchanged across different samples. As the edge feature matrix is not a variable, it is not included in Figure 4 b).

After downsampling, the features then go through another Re-MP layer with P_c message passing steps. This layer performs message passing on the coarsened graph, while updating the coarse-layer-hidden-state matrix \mathbf{H}_c . As the coarse graph is much smaller, P_c can be selected to be larger than P_f without significant sacrifice in performance. The updated features are then upsampled with a set of upsampling layers that are symmetrical to the downsampling layers. Before each upsampling layer, a skip connection is employed to promote long-range information passing, forming a U-Net architecture. The final upsampled node feature $\mathbf{X}_V^{l_0}$ are processed with P_f steps of message passing by a Re-MP layer together with hidden state \mathbf{H}_f and the previously updated edge feature $\mathbf{X}_E^{l_0}$. The outputs of this layer are then fed into the decoder, returning the final nodal prediction of the current time step, which is the incremental displacement fields of each node. This is also the nodal input for the next time step, $\mathbf{X}_V^{t_{i+1}}$, for autoregressive predictions. The edge feature of the next time step, $\mathbf{X}_E^{t_{i+1}}$, can be calculated based on the deformed shape of the component.

3.3.2 Encoder and Decoder

Similar to GNS [30], the graph features are encoded into latent space with a channel number of C_{en} by the encoder. Specifically, the node and edge features are encoded with 2 MLP sequences, consisting of 4 fully connected layers followed by the ReLU activation function. Layer normalisation is employed to improve stabilisation during training. The encoder can be defined as:

$$\mathbf{X}_V^{en} = \text{MLP}_{NodeEncoder}(\mathbf{X}_V), \quad \mathbf{X}_E^{en} = \text{MLP}_{EdgeEncoder}(\mathbf{X}_E), \quad (2)$$

where \mathbf{X}_V^{en} and \mathbf{X}_E^{en} are the encoded node and edge features respectively.

The decoder also utilises the same MLP sequence structure, which decodes the updated features into the final output dimension. For a node prediction task, only node decoder is used in this architecture to output the node feature prediction for the next time steps.

3.3.3 Recurrent message passing layer

As illustrated in Figure 4, the recurrent message passing (Re-MP) layer is employed in both the finest level l_0 and the coarsest level l_3 of the U-Net. The purpose of the first Re-MP layer is to aggregate information before the downsampling steps. The reason is that, geometric information is only encoded as edge features. In order to perform spatial computations at the coarse scale, this information has to first be integrated into the node feature vectors as the downsampling operator only passes node features to the next level. In addition, the Re-MP layer can aggregate and encode important non-smooth local features, which could otherwise get lost in the downsampling process. Because of the excessive number of edges in the fine graph, the number of message passing steps P_f in this layer should be minimised to improve overall model efficiency.

The Re-MP layer in the coarsest level serves the purpose of a bottleneck in the architecture. This layer propagates and updates the concentrated node features through P_c message passing steps to model the mapping between input and output features. Because of the reduced number of edges, message passing

in this layer is highly efficient and a larger P_c can be selected. Detailed hyper parameter tuning will be explained in Section 5. Another Re-MP layer is employed after upsampling to the finest level while referring to the initial features using a skip connection.

Each Re-MP layer consists of an edge block and a node block, updating the edge and node features iteratively. As the name suggests, the Re-MP layer introduces the recurrent operation across time steps by updating the hidden state. Two sets of hidden states are propagated through time: one at the finest level \mathbf{H}_f , and the other at the coarsest level of the U-Net \mathbf{H}_c . The hidden state matrices are input into the edge block together with the input features. Within each iteration of message passing, the features first pass through the edge block updating the edge information and the hidden state. The detailed algorithm for the edge block can be explained as:

$$\mathbf{X}'_E = \text{MLP}_{Edge}(\mathbf{X}_{V_s}, \mathbf{X}_{V_r}, \mathbf{X}_E, \mathbf{H}), \quad \mathbf{H}' = \text{MLP}_{Hidden}(\mathbf{X}_{V_s}, \mathbf{X}_{V_r}, \mathbf{X}_E, \mathbf{H}), \quad (3)$$

where \mathbf{X}'_E is the updated edge feature matrix, \mathbf{X}_{V_s} and \mathbf{X}_{V_r} are the node feature matrices of the sender and receiver nodes of all edges, $\mathbf{H} \in \mathbb{R}^{N \times p_e}$ is the hidden state, and \mathbf{H}' is the updated hidden state. Note that the hidden state has the same dimension as the edge feature matrix, which is initialised to $\mathbf{0}$ at time t_1 and is updated iteratively at each time step to propagate local historical information. The updated edge information is then used in the node block for aggregating and updating the node features, which can be described as:

$$\mathbf{X}_V^{\text{agg}}[v_n] = \sum_{e_m \in E(v_n)} \mathbf{X}'_E[e_m], \quad \mathbf{X}'_V = \text{MLP}_{Node}(\mathbf{X}_V, \mathbf{X}_V^{\text{agg}}), \quad (4)$$

where $E(v_n)$ is the set of edges connecting an arbitrary node v_n .

Multiple message passing steps within a graph is achieved by stacking a sequence of Re-MP layers. The number of message passing steps in each Re-MP layer is tuned as a hyperparameter, which is discussed in detail in Section 5.2. When the number of layers increases, the model may suffer from the vanishing gradient problem. To accommodate this, residual connection is added in each Re-MP layer by combining the input and output at each layer.

3.3.4 Downsampling and upsampling layers

As previously mentioned, the coarsened graphs are constructed using software generated FE meshes, which are shared across all samples within the dataset. However, each sample contains a geometry with a unique shape design, leading to a unique mesh configuration that may have varying numbers of in-graph edges. Therefore, when downsampling from the original graph to the first coarsened graph, the number of cross-graph edges varies among samples. Conversely, when downsampling between the shared coarsened graphs, the number of cross-graph edges remains constant. To accommodate this, two distinct types of downsampling / upsampling layers are utilised within the architecture, namely the message passing down/upsampling layer and the non-shareable weight down/upsampling layer.

The message passing downsampling (DS-MP) layer is similar to the Re-MP layer which performs message passing within a graph. A DS-MP layer propagates node features from the fine graph to the coarse graph through the cross-graph edges using their edge features consisting of 4 channels, the relative distances in the x, y, and z directions, and the Euclidean distance. Each DS-MP layer only performs one iteration of message passing, hence residual connection is not employed.

After the first downsampling layer, non-shareable weight downsampling (DS-NW) layers are used for downsampling between the coarsened graphs. Inspired by the MAg layer [13], DS-NW first assigns a unique weight vector to each edge for feature update, making the weight matrix non-shareable. The assignment of a unique weight to each edge allows a more tailored aggregation of features, enabling the model to capture and adapt to more complex patterns within the data. The weight matrix can be denoted as $\mathbf{W} \in \mathbb{R}^{M \times C_{in} \times C_{out}}$, where M is the number of edges, C_{in} and C_{out} are the input and output channel number to the layer. Similar to a standard U-Net, each downsampling layer increases the channel number by a factor of 2. DS-NW is especially suitable for feature aggregation with large channel numbers as it assigns channel-wise weights to each edge. DS-NW then aggregates the updated features to the neighbouring nodes. The algorithms can be expressed as:

$$\mathbf{x}'_{e_{v_s, v_r}} = \sum_{c \in C_{in}} \mathbf{x}_{v_s}^{(c)} \cdot \mathbf{w}_{e_{v_s, v_r}}^{(c)}, \quad \mathbf{X}_{V_r}^{\text{agg}}[v_r] = \text{LeakyReLU} \left(\sum_{v_s \in N(v_r)} \mathbf{x}'_{e_{v_s, v_r}} \right), \quad (5)$$

where $\mathbf{x}'_{e_{v_s, v_r}} \in \mathbb{R}^{C_{out}}$ is the updated node features propagated through the edge connected from the sender node v_s to the receiver node v_r , $\mathbf{x}_{v_s}^{(c)}$ is the c -th channel component of the node feature vector \mathbf{x}_{v_s} , $\mathbf{w}_{e_{v_s, v_r}}^{(c)} \in \mathbb{R}^{C_{out}}$ is the c -th channel component of the weight matrix $\mathbf{W}_{e_{v_s, v_r}}$ corresponding to edge e_{v_s, v_r} , $\mathbf{X}_{V_r}^{\text{agg}} \in \mathbb{R}^{N_{V_r} \times C_{out}}$ is the final aggregated node feature matrix of all the receiver nodes, $N(v_r)$ is the set of sender nodes that are connected to the receiver node v_r . The aggregated features are then fed through a LeakyReLU activation function to introduce nonlinearity.

The advantage of DS-NW compared to DS-MP is that the non-shareable weight matrix enables more accurate yet straightforward feature updates for multi-channel calculations. Each unique weight component is fully trainable, enhancing performance while maintaining high efficiency. However, this approach has poor generalisability as it requires the number of edges M to be constant. A trained weight matrix cannot be directly used on other samples with different M . Therefore, DS-NW is only applicable for downsampling and upsampling between the commonly shared coarsened graphs. In contrast, DS-MP updates features based on MLPs, therefore can be applied to a variable number of edges, regardless of the graph size. The consideration of edge features before aggregation further enhances the generalisability of this approach. As a result, the message passing downsampling / upsampling layers are used at the finest level, and the non-shareable weight approach is applied to the coarser levels.

4 Data acquisition

The dataset used for training the model is generated using FE simulations. A hot stamped steel B-pillar is evaluated with side impact test. The FE model aims to simulate a simplified crash test that only operates on the B-pillar at a component level [36]. As illustrated in Figure 5 a), the B-pillar is fixed at its upper and lower extremities, with a hemispherical impactor positioned to strike at the lower region, simulating a vehicle side crash scenario. Figure 5 b) shows the FE setup of the impact test, fixed boundary conditions in all six degrees of freedom are applied to the top and bottom ends of the B-pillar, and the impactor collides with the component with an initial velocity in the negative z direction. The resultant displacement fields are extracted, which depict the deformation and collapse mode during impact. Figure 5 c) shows an example of the z -displacement field.

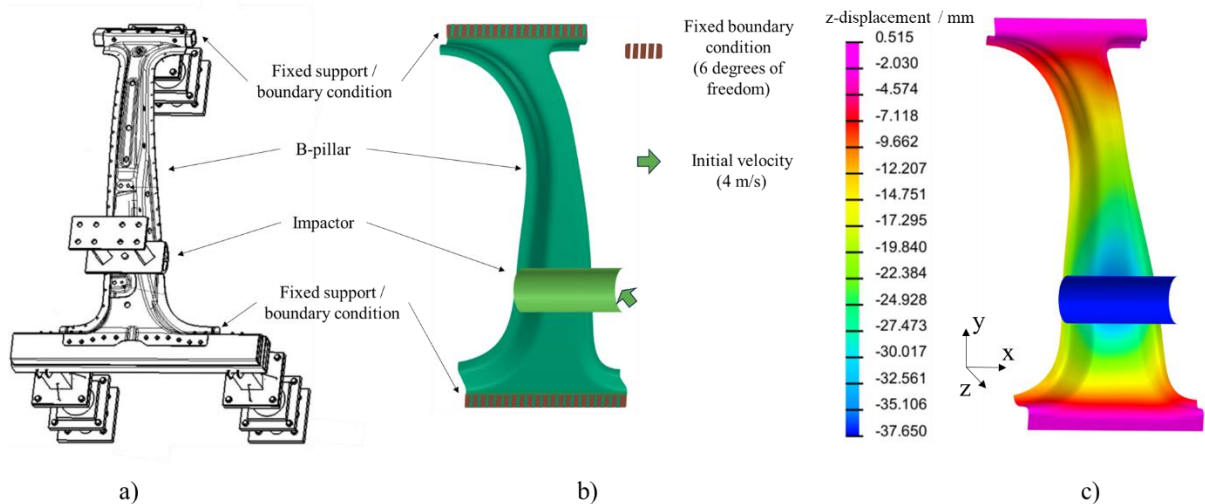


Figure 5: Illustration of a) experimental setup of the B-pillar impact test [36], b) FE setup of the B-pillar impact test, and c) result contour of the FE simulation.

In order to study the influence of designed shape on the crashworthiness performance, the material properties, boundary and loading conditions remain constant throughout all samples. Specifically, the initial position of the impactor is adjusted on top of the geometry without any offset according to the

mesh morphing to ensure constant loading condition. The FE model of the B-pillar is a scaled-down representation, approximately one-third the size of a full-scale B-pillar component used in real-world applications. Correspondingly, the impactor is proportionally scaled down by the same factor, maintaining the same size ratio. The length of the B-pillar is 350 mm, the impactor has a diameter of 40 mm and a mass of 100 kg, and the initial impact velocity is 4 m/s.

The material of the B-pillar is defined to be boron steel with the 100% martensite phase under room temperature, which is a strain-rate dependent material. Its property is defined with the constitutive model developed by Li [37], then input into PAM-CRASH as look-up table. Figure 6 shows the relationship between true stress and true strain of the material at four representative strain rates. Note that the damage mechanism is excluded from the material model to enhance the numerical stability of the FE simulations. This approach is commonly applied in crash simulations, where damage evolution is typically less critical than the plastic behaviour of the B-pillar component during side impact tests.

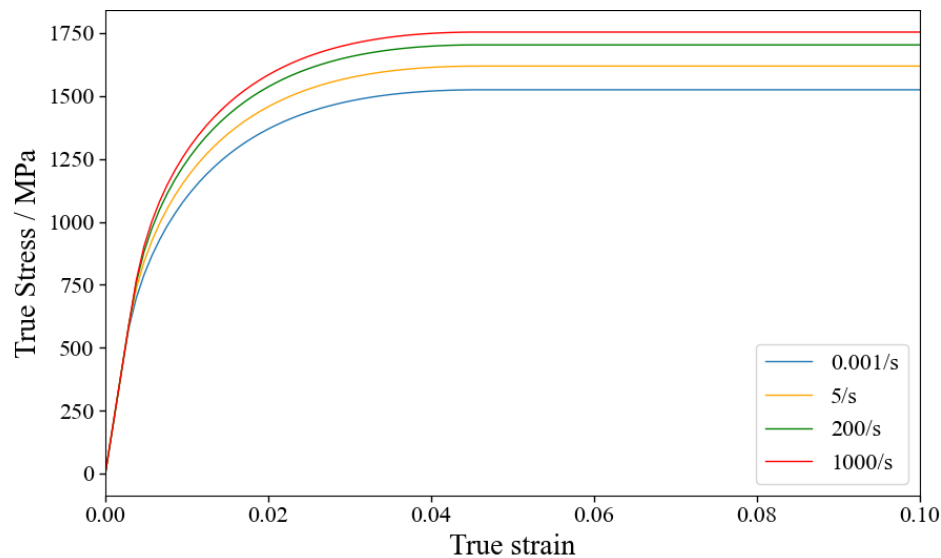


Figure 6: Material properties of the boron steel with different strain rates under room temperature.

When constructing graph sequences from the dynamic simulations, the entire crash duration is divided into 12 time steps, with each step separated by an equally spaced time interval of 1.5 ms. This allows for consistent temporal analysis throughout the simulation, ensuring that the progression of the deformation can be accurately modelled and captured at uniform time intervals.

The design modification is made through mesh morphing, which alters the shape of the component by directly manipulating its geometry. As shown in Figure 7, the B-pillar is morphed in the z direction at one of the three control points defined on the component. The morphing distance is controlled to remain within $\pm 8\%$ of the total thickness in the z-direction of the baseline B pillar. Latin hypercube sampling (LHS) is used to randomly sample both the control point variable and the morphing distance, ensuring a comprehensive exploration of the design space while maintaining a uniform distribution of the sampled variables. Three sets of data are generated with separate LHS operations for training, validation, and testing, each covering the entire design space. This ensures that every dataset has diverse and representative samples from the design space. The training set contains 100 samples, while the validation and test sets each consists of 50 samples. Each sample consists of a graph sequence of 12 graphs including the initial state, representing the intermediate frames at each time step throughout the crash simulation.

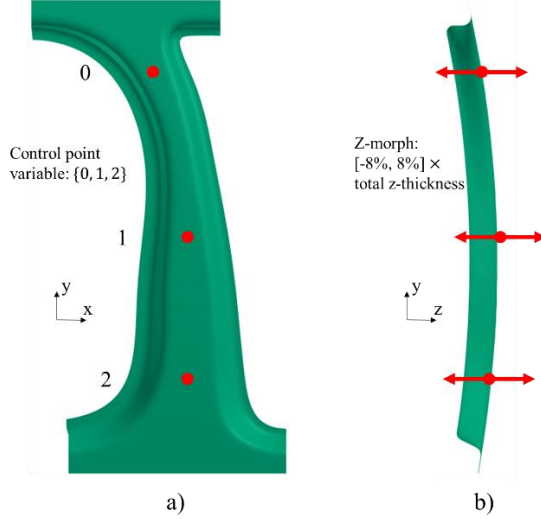


Figure 7: Morphing variables of the B-pillar component.

5 Results and discussion

ReGUNet is trained using a teacher forcing approach, where at each time step, the model's predictions are based on the ground truth input from the graph sequence, rather than on its own previous prediction. This training technique helps guide the model by providing correct intermediate inputs, which aids in faster learning and reduces the risk of accumulating errors during training. The mean square error (MSE) is used as the loss function during training. However, during model evaluation, the model relies on its own predictions in an autoregressive inference mode. This means that only the initial graph from every sequence is provided to the model, which is used by the model to predict the second graph. The model subsequently uses its own prediction of the second graph to generate the third graph, and this process continues iteratively until the end of the entire sequence.

5.1 Baseline model comparisons

ReGUNet is compared with three Baseline models to evaluate its performance. Baseline 1 is an encoder-processor-decoder-based GN model which is adopted in both GNS [30] and MGN [23]. Baseline 2 is a customised GN model that incorporates recurrence between time steps similar to ReGUNet. The key difference between Baseline 2 and ReGUNet is that Baseline 2 operates only on the original graph without any downsampling. Baseline 3 has a similar U-Net architecture as ReGUNet, but without hidden state propagation between time steps. The comparison between the four models enables a clear visualisation of the performance improvement by introducing downsampling layers and hidden state propagation.

For all four models, the training hyperparameters are kept constant to ensure that all control variables remain unchanged, allowing reproducible and unbiased comparisons. The batch size is set to 2, the learning rate is 0.0004 for the first 500 epochs and reduced to 0.0002 for the remaining. For Baseline 1 and 2, the encoder encodes all features to a latent dimension with 128 channels; the number of message passing steps is 15. Whereas for Baseline 3 and ReGUNet, the channel number is 16 after the encoder, which increases by a factor of 2 for each downsampling layer, reaching 128 at the coarsest layer; the number of message passing steps is 1 at the finest layer and 15 at the coarsest layer.

All models are trained for 800 epochs in a teacher forcing manner, but are evaluated with autoregressive inference after training. In the autoregressive inference mode, the deviation between the predicted graph and the ground truth graph naturally increases over time due to error accumulation. As the model uses its previous predictions as inputs for the next step, small errors from earlier predictions propagate and amplify, leading to a greater discrepancy as time progresses. The prediction accuracy is evaluated by calculating the mean Euclidean distance for all nodes between ground truth and prediction during each time step. Figure 8 shows the error accumulation of both training and validation data for the four models over 12-time steps. The error at each time step is calculated by averaging the mean Euclidean distance

between ground truth and prediction across the whole dataset. One can observe that the baseline models have significantly larger error accumulation during autoregressive inference compared to ReGUNet.

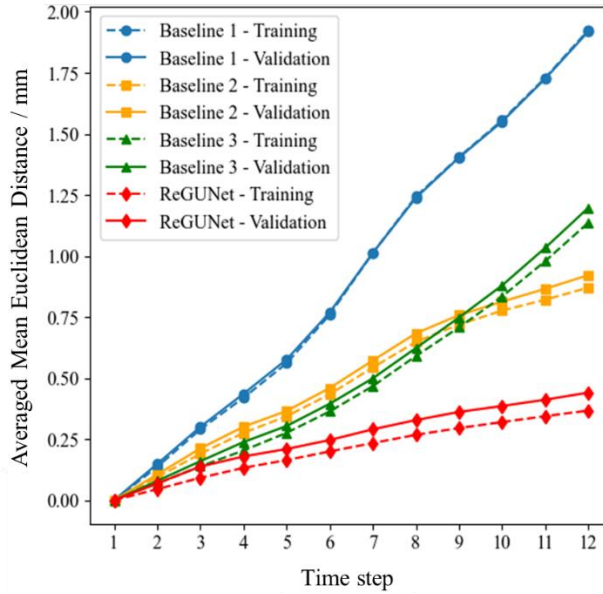


Figure 8: Comparison between the four models in terms of error accumulation over 12 time steps.

As seen in Figure 8, Baseline 2 and ReGUNet has a notable decrease in the gradient of error accumulation compared to the other models. Despite earlier time steps, the prediction errors of Baseline 3 are smaller than those of Baseline 2, at later time steps, the errors of Baseline 3 surpass that of Baseline 2. This indicates that Baseline 3 experiences greater error accumulation as the sequence progresses. The key difference between them is the utilisation of recurrence over time steps. This suggests that both Baseline 2 and ReGUNet handle long-term predictions more effectively, with slower error growth over time, due to the propagation of hidden state which contains historical information. Figure 8 also indicates a clear improvement in model performance due to graph downsampling. This can be observed in the comparisons between Baseline 1 and Baseline 3, as well as between Baseline 2 and ReGUNet, as the latter models exhibit slower error growth and lower error values over all timesteps.

Figure 9 shows the comparisons between ground truth and prediction at the final time step for all four models in terms of total z-displacement contour plots. One representative validation data sample is selected for this illustration. Two insightful points can be observed from the illustration.

Firstly, for Baselines 1 and 2, both operating only on the fine graph without downsampling, the error distributions appear to be more concentrated compared to the other two models, where large regions with errors of the same sign can be observed. This is because of insufficient message passing steps in these models. To propagate messages to physically distant nodes, significantly more message passing steps are required in fine graphs compared to coarse graphs due to higher node density with shorter edge connections. With 15 message passing steps, the distance information can travel in fine graphs is very limited, leading to less accurate prediction. Further increasing the number of message passing steps can result in a significant increase in GPU memory and inference time. In contrast, for Baseline 3 and ReGUNet, the 15 message passing steps cover a longer range in the coarsened graph. With a longer message passing range, the node feature updates incorporate information from a broader neighbourhood, allowing a more comprehensive understanding of the graph's overall structure. This is the primary reason why graph downsampling contributes to enhanced accuracy.

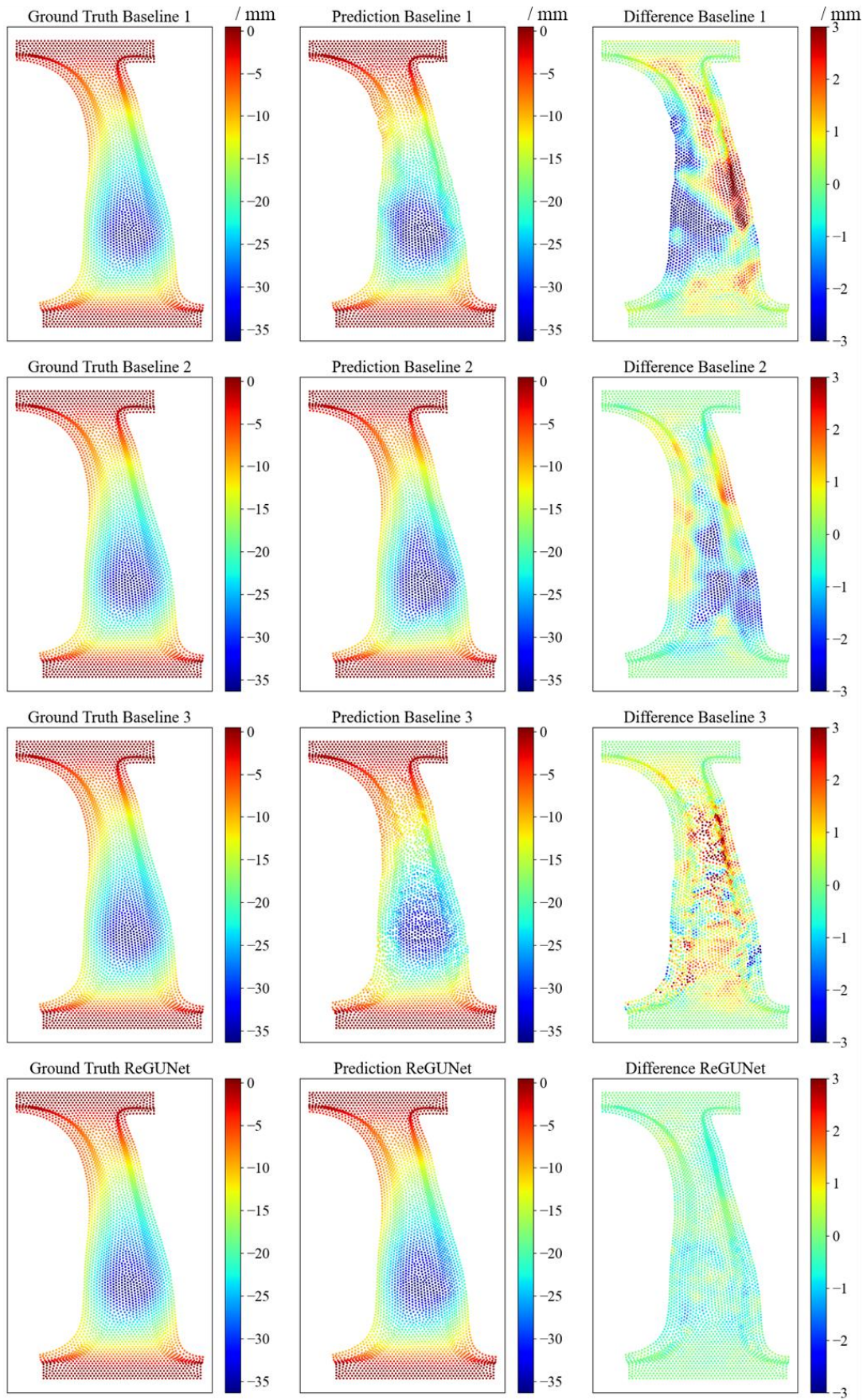


Figure 9: Comparisons between the four models in terms of total z-displacement contour plots of a validation sample.

Secondly, one can easily notice severe scatter errors that cause random waviness in the final predicted graphs for Baselines 1 and 3. These models, which lack recurrence between time steps, show greater inconsistencies in their predictions, leading to less smooth graph structures. Unlike the macroscopic error distribution caused by insufficient message-passing steps, these errors primarily affect local feature predictions. They arise from the accumulation of small errors over time, which become significant at later time steps. These small errors, occurring in multiple directions, lead to a wavy and scattered graph structure that becomes increasingly irregular as time progresses. The recurrence of hidden states, which contains historical information from previous time steps, helps mitigate the accumulation of errors over time. Therefore, models with recurrence are able to produce smoother graph structure predictions.

Table 1 summarises the comparison among the four models in terms of efficiency and accuracy. The training is conducted using an Nvidia A100 GPU on Google Colab. One can observe that, without graph downsampling, the GPU RAM consumption increases significantly. This is because fine graphs have a much larger number of nodes and edges, leading to greater memory usage for processing and storing intermediate computations during message passing. Downsampling reduces the complexity of the graph, which in turn lowers the memory requirements, making the model more resource-efficient and scalable, especially for large-scale graphs. On the other hand, the presence of recurrence has a relatively smaller impact on model efficiency. While adding recurrence slightly increases GPU consumption and extends training time, the boost in accuracy is substantial. The trade-off between the minor increase in computational demand and the significant improvement in accuracy makes recurrence a valuable feature for enhancing the model's performance. In comparison to Baseline 3, a reduction by 63% in terms of mean validation error at the final time step is achieved by introducing recurrence mechanism. While compared to Baseline 2, the employment of graph downsampling leads to an accuracy enhancement of 51% with significantly improved computational efficiency. Overall, ReGUNet demonstrates the most promising performance among all four models.

Table 1: Overall comparisons between the four models.

	GPU memory / GB	Time per epoch / min	Mean validation error / mm
Baseline 1	15.9	1.00	1.92
Baseline 2	20.3	1.24	0.92
Baseline 3	8.7	1.14	1.20
ReGUNet	9.5	1.25	0.45

5.2 Hyperparameter tuning

To achieve the best performance with ReGUNet, it is essential to determine the optimal combination of hyperparameters, including the numbers of message passing layers P_f and P_c , the number of cross-graph edges per node between finer and coarser layer k , and the channel numbers. The model is trained with different combinations of hyperparameters with Nvidia T4 GPU with 16 GB RAM provided by Google Colab.

Firstly, the effect of channel number on model performance is studied. The channel number output from the encoder is varied between 16, 32, 64. After 2 non-shareable weight downsampling layers, the channel number at the coarsest level reaches 64, 128, 256. Table 2 summarises the model's efficiency and accuracy with different channel numbers. The message passing steps are kept constant at $P_f = 1$ and $P_c = 15$; the number of cross-graph edges per node is kept at $k = 6$. When the channel numbers increase to 64 - 256, the GPU memory consumption exceeds the limit of 16 GB, making the model inexecutable. Comparing 16 - 64 and 32 - 128, the latter leads to a lower validation error despite an insignificant trade-off in efficiency in terms of both GPU memory and training time. Therefore, 32 - 128 is selected for further calibrations.

Table 2: The effect of channel number on model performance.

Channel numbers	GPU memory / GB	Time per epoch / min	Mean validation error / mm
16 - 64	6.7	1.02	0.66
32 - 128	9.5	1.24	0.45
64 - 256	>16	N/A	N/A

Next, four values of k between 3 and 12 are tested to determine the optimal number of cross-graph edges. With more cross-graph edges between two graphs, the receiver nodes receive information from a larger number of sender nodes. As before, P_f and P_c are kept at 1 and 15 respectively. Table 3 and Figure 10 show the effect of k on model performance in terms of validation accuracy and efficiency. One can observe that when k exceeds 6, both training time and memory consumption increase rapidly, however, the reduction in validation error gradually diminishes. This suggests that while increasing k initially improves the model's accuracy, beyond a certain point, the computational costs outweigh the performance gains. As a result, $k = 6$ is chosen for further calibration.

Table 3: The effect of number of cross-graph edges per sender node on model performance.

k	GPU memory / GB	Time per epoch / min	Mean validation error / mm
3	7.6	1.39	0.57
6	8.5	1.40	0.45
9	9.2	1.48	0.42
12	9.5	1.63	0.40

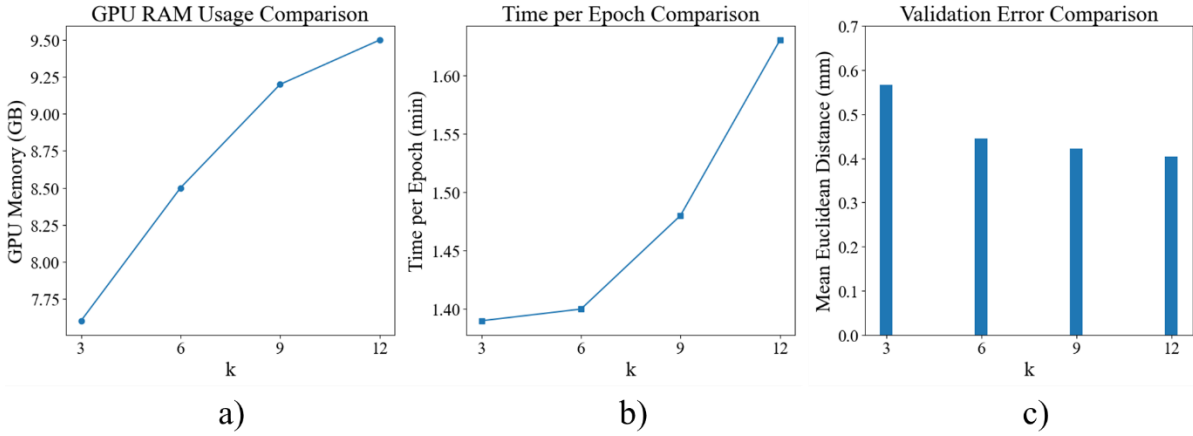


Figure 10: Illustrations of the effect of number of cross-graph edges per sender node on model performance, in terms of a) GPU memory consumption, b) training time, and c) validation error.

Lastly, the optimal numbers of message passing steps P_f and P_c are determined. Eight combinations of message passing steps are evaluated, where P_c taking values of 5, 10, 15, and 20, P_f is set to 1 and 2. A larger P_f will result in memory consumption exceeding the available limit. This is because message passing on fine graphs is more computationally expensive. Table 4 and Figure 11 summarise the relationship between message passing steps and model performance. One can observe that when $P_f = 2$, the validation error decreases, with a slight increase in training time. For P_c , 10 message passing steps shows the best prediction accuracy with the lowest GPU memory consumption. Meanwhile, the training time is significantly lower than that when P_c is 15 and 20. The reason why more message passing steps leads to a higher error may be due to the oversmoothing problem. This occurs when, after a certain number of layers, the node features become increasingly similar, making it difficult for the model to distinguish between different nodes. As message passing continues, the node features converge, homogenising the node representations and reducing the model's ability to capture local

differences. As a result, 2 and 10 message passing steps for the fine and coarse levels are selected as the final optimised parameters.

Table 4: The effect of numbers of message passing steps on model performance.

	GPU memory / GB		Time per epoch / min		Mean validation error / mm	
	$P_f = 1$	$P_f = 2$	$P_f = 1$	$P_f = 2$	$P_f = 1$	$P_f = 2$
$P_c = 5$	7.3	9.2	0.76	0.98	0.40	0.36
$P_c = 10$	7.0	9.6	1.10	1.26	0.38	0.30
$P_c = 15$	8.5	10.1	1.40	1.63	0.45	0.36
$P_c = 20$	8.7	10.1	1.73	1.86	0.44	0.34

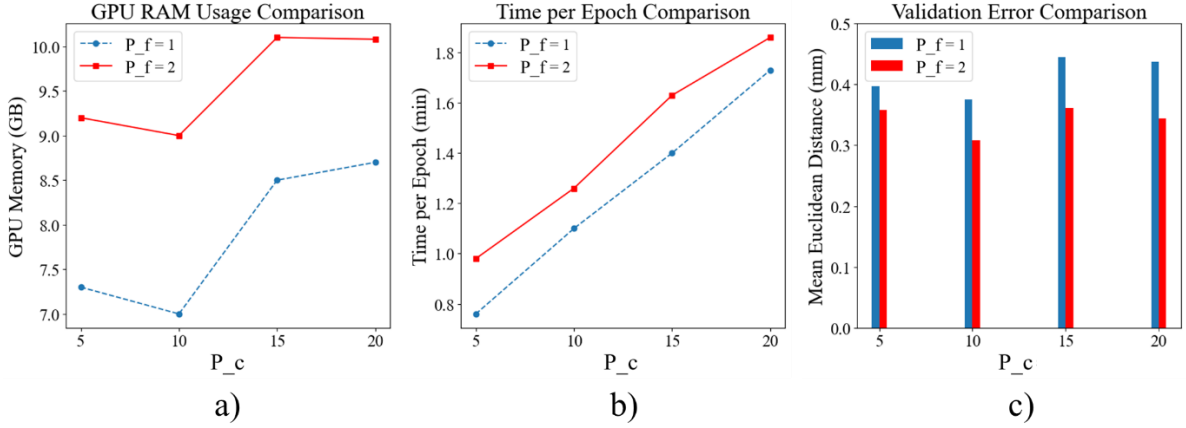


Figure 11: Illustrations of the effect of numbers of message passing steps on model performance, in terms of
 a) GPU memory consumption, b) training time, and c) validation error

Finally, the model with 6 cross-graph edges per sender node, channel numbers of 32 - 128, and message passing steps of 2 and 10 in the fine and coarse levels, is selected as the final tuned model. Figure 12 first compares the error accumulation of the tuned and untuned model for the training set and validation set. In comparison to the untuned model, the error accumulation is significantly reduced, indicating that the tuning process has effectively enhanced the model's performance by minimising the propagation of errors, resulting in more accurate and consistent predictions. In addition, the tuned model is further evaluated with the test set. The averaged error accumulation across the test set is also plotted in Figure 12. One can observe that compared to the validation set, there is a very slight increase in terms of mean Euclidean distance at later time steps, reaching a final test error of 0.32 mm. This demonstrates the model's ability to generalise and make accurate predictions on previously unseen samples.

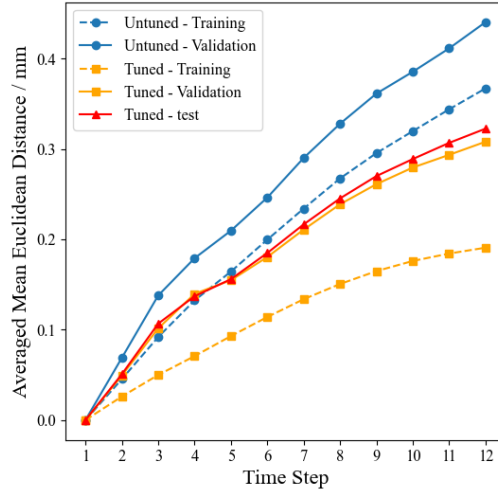


Figure 12: Error accumulation of the ReGUNet after hyperparameter tuning.

Figure 13 shows representative samples in the test set showing the prediction of the total z-displacement field of the B-pillar. One can observe good agreement between the ground truth and prediction. Also, the model is able to capture the change in resultant deformation fields given the variation in component design. One of the key metrics used to evaluate crashworthiness performance is the maximum B-pillar intrusion, which is defined as the maximum z-displacement of the B-pillar during a crash test. This is the maximum z-displacement value extracted from the final time step for each sample. The maximum percentage error of the maximum B-pillar intrusion among the test set is 0.74%. Full prediction of the dynamic behaviour of a representative sample of the test set is plotted in the Appendix.

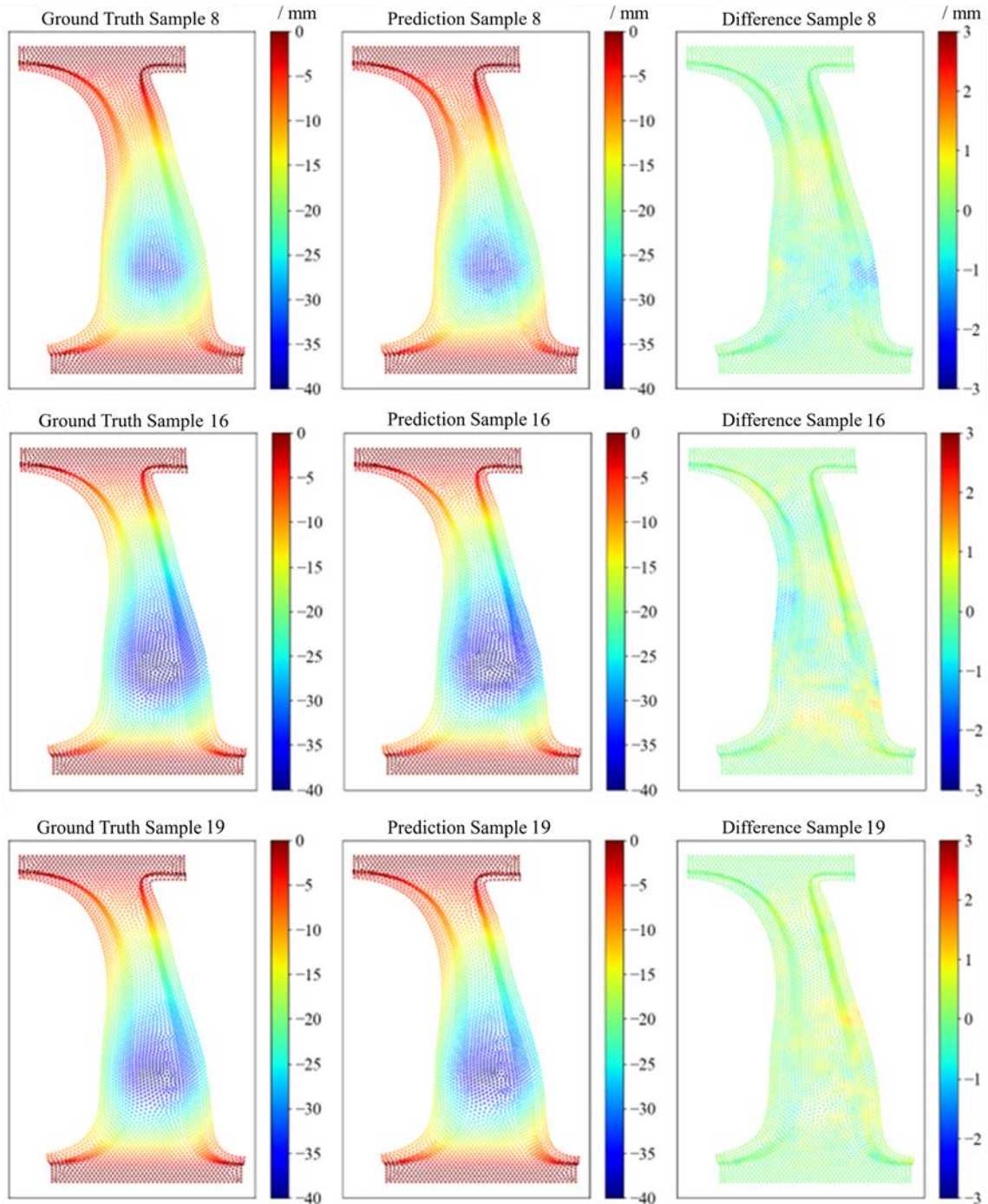


Figure 13: Differences between ground truth and prediction of total z-displacement of representative test samples.

6 Conclusions

In this paper, a GNN-based surrogate model, Recurrent Graph U-Net (ReGUNet) is proposed to predict the dynamic behaviour of vehicle panel components under side crash simulations. The model operates on graph-structured data, which is naturally a well-suited representation form of mesh data. Graph nodes can represent nodes in a mesh, while edges capture the connections between them. To enable more efficient message passing between distant nodes, graphs are downsampled by generating coarsened meshes of the geometry. Multiple layers of coarsened graphs with different node densities are created to establish a U-Net architecture. Specialised downsampling and upsampling layers are employed for efficient and accurate message passing between graphs at different levels. Within the finest and coarsest levels, recurrent message passing layers are utilised to enable message passing within the graphs in a recurrent manner. Message passing at the coarsest level can propagate feature information over a longer distance with fewer message passing steps, capturing spatial long-range dependencies between nodes. Each recurrent message passing layer not only performs information propagation within the graphs, but also propagates hidden states that contain historical information of previous time steps. This recurrence mechanism leads to more stabilised predictions over a larger number of time steps. The comparison between ReGUNet and three baseline models showcases the benefits of incorporating graph downsampling and recurrent architecture in the model by a prediction improvement of more than 51%. The ReGUNet model is further tuned with hyperparameters and evaluated on previously unseen test data. The results demonstrate the model's accurate and efficient prediction performance in capturing the dynamic deformation behaviour of various B pillar components throughout entire crash simulations. At the final time step, the model is capable of predicting the maximum B-pillar intrusion within a maximum relative error of 0.74%.

ReGUNet, as a new graph-based surrogate model, shows great potential in rapid predictions of other crashworthiness indicators, such as crash force distribution and specific energy absorption. In the future, the model can be used to perform more comprehensive crashworthiness analyses for more complex components. It can also be employed to establish a graph-based optimisation platform for crashworthiness-performance-driven optimal design of vehicle panel components.

References

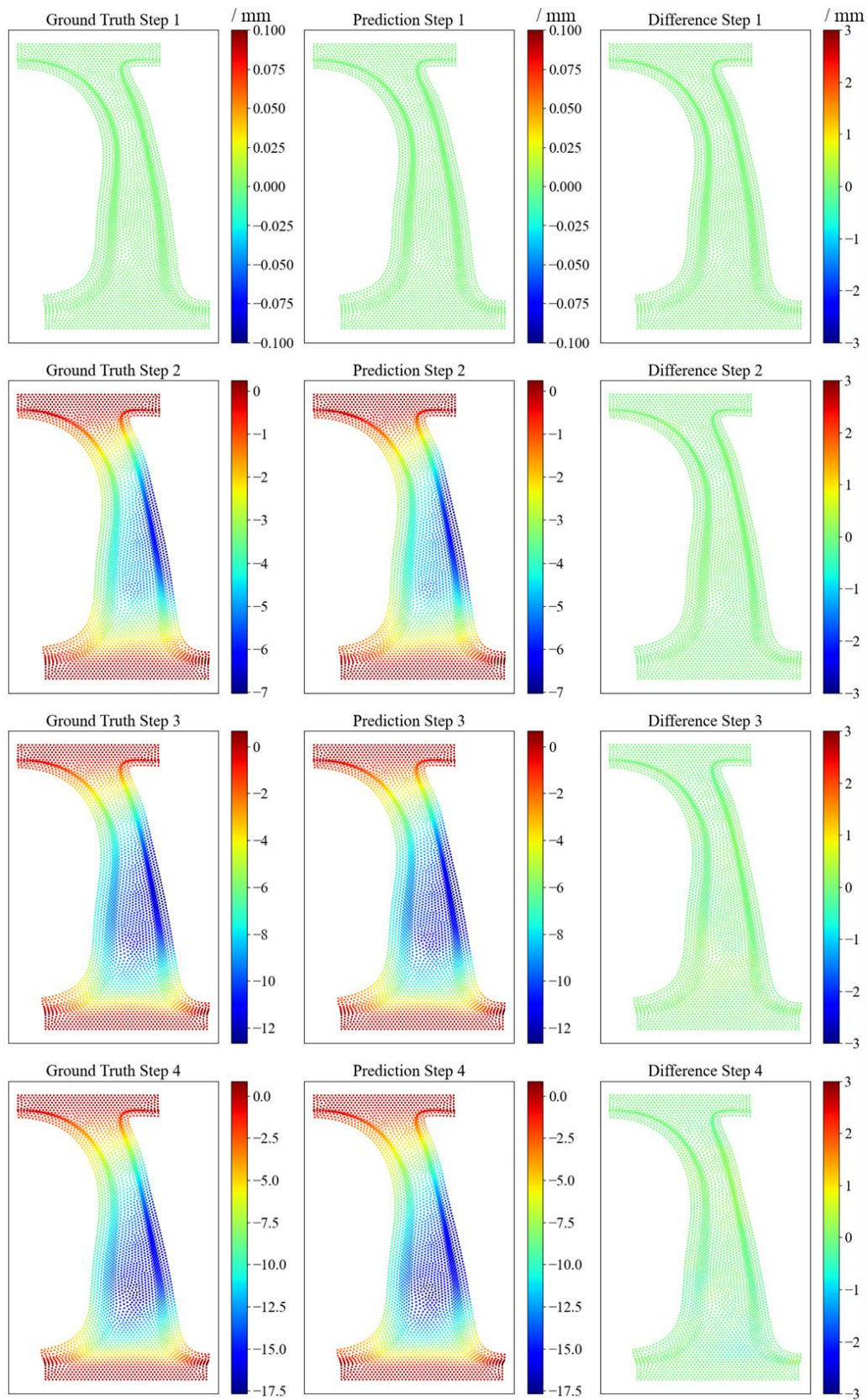
1. Kim, H.C. and T.J. Wallington, *Life-Cycle Energy and Greenhouse Gas Emission Benefits of Lightweighting in Automobiles: Review and Harmonization*. Environmental Science & Technology, 2013. **47**(12): p. 6089-6097.
2. IIHS, *Side Impact Crashworthiness Evaluation 2.0 Crash Test Protocol*. 2022, Insurance Institute for Highway Safety.
3. Rogala, M., J. Gajewski, and M. Ferdynus, *The Effect of Geometrical Non-Linearity on the Crashworthiness of Thin-Walled Conical Energy-Absorbers*. Materials, 2020. **13**(21): p. 4857.
4. Sakaridis, E., N. Karathanasopoulos, and D. Mohr, *Machine-learning based prediction of crash response of tubular structures*. International Journal of Impact Engineering, 2022. **166**.
5. Albak, E.İ., *Optimization design for circular multi-cell thin-walled tubes with discrete and continuous design variables*. Mechanics of Advanced Materials and Structures, 2023. **30**(24): p. 5091-5105.
6. Ahmadi Dastjerdi, A., et al., *Crushing analysis and multi-objective optimization of different length bi-thin walled cylindrical structures under axial impact loading*. Engineering Optimization, 2019. **51**: p. 1-18.
7. Zende, P. and H. Dalir. *Multi-Objective Optimization of Composite Square Tube for Minimizing Peak Crushing Force and Maximizing Specific Energy Absorption Using Artificial Neural Network and Genetic Algorithm*. in *ASME International Mechanical Engineering Congress and Exposition, Proceedings (IMECE)*. 2022.
8. Xiong, F., et al., *Multi-objective lightweight and crashworthiness optimization for the side structure of an automobile body*. Structural and Multidisciplinary Optimization, 2018. **58**(4): p. 1823-1843.
9. Kohar, C.P., et al., *Using Artificial Intelligence to Aid Vehicle Lightweighting in Crashworthiness with Aluminum*. MATEC Web Conf., 2020. **326**: p. 01006.
10. Guo, W., et al., *Machine learning-based crashworthiness optimization for the square cone energy-absorbing structure of the subway vehicle*. Structural and Multidisciplinary Optimization, 2023. **66**(8): p. 182.
11. Kohar, C.P., et al., *A machine learning framework for accelerating the design process using CAE simulations: An application to finite element analysis in structural crashworthiness*. Computer Methods in Applied Mechanics and Engineering, 2021. **385**.
12. Li, H., H. Zhou, and N. Li, *An integrated convolutional neural network-based surrogate model for crashworthiness performance prediction of hot-stamped vehicle panel components*. MATEC Web of Conferences, 2024. **401**.
13. Deshpande, S., J. Lengiewicz, and S. Bordas, *MAGNET: A Graph U-Net Architecture for Mesh-Based Simulations*. arXiv preprint arXiv:2211.00713, 2022.
14. He, J., et al., *On the use of graph neural networks and shape-function-based gradient computation in the deep energy method*. International Journal for Numerical Methods in Engineering, 2023. **124**(4): p. 864-879.
15. Fu, X., et al., *An finite element analysis surrogate model with boundary oriented graph embedding approach for rapid design*. Journal of Computational Design and Engineering, 2023. **10**(3): p. 1026-1046.
16. Chen, Q., et al., *Predicting dynamic responses of continuous deformable bodies: A graph-based learning approach*. Computer Methods in Applied Mechanics and Engineering, 2024. **420**: p. 116669.

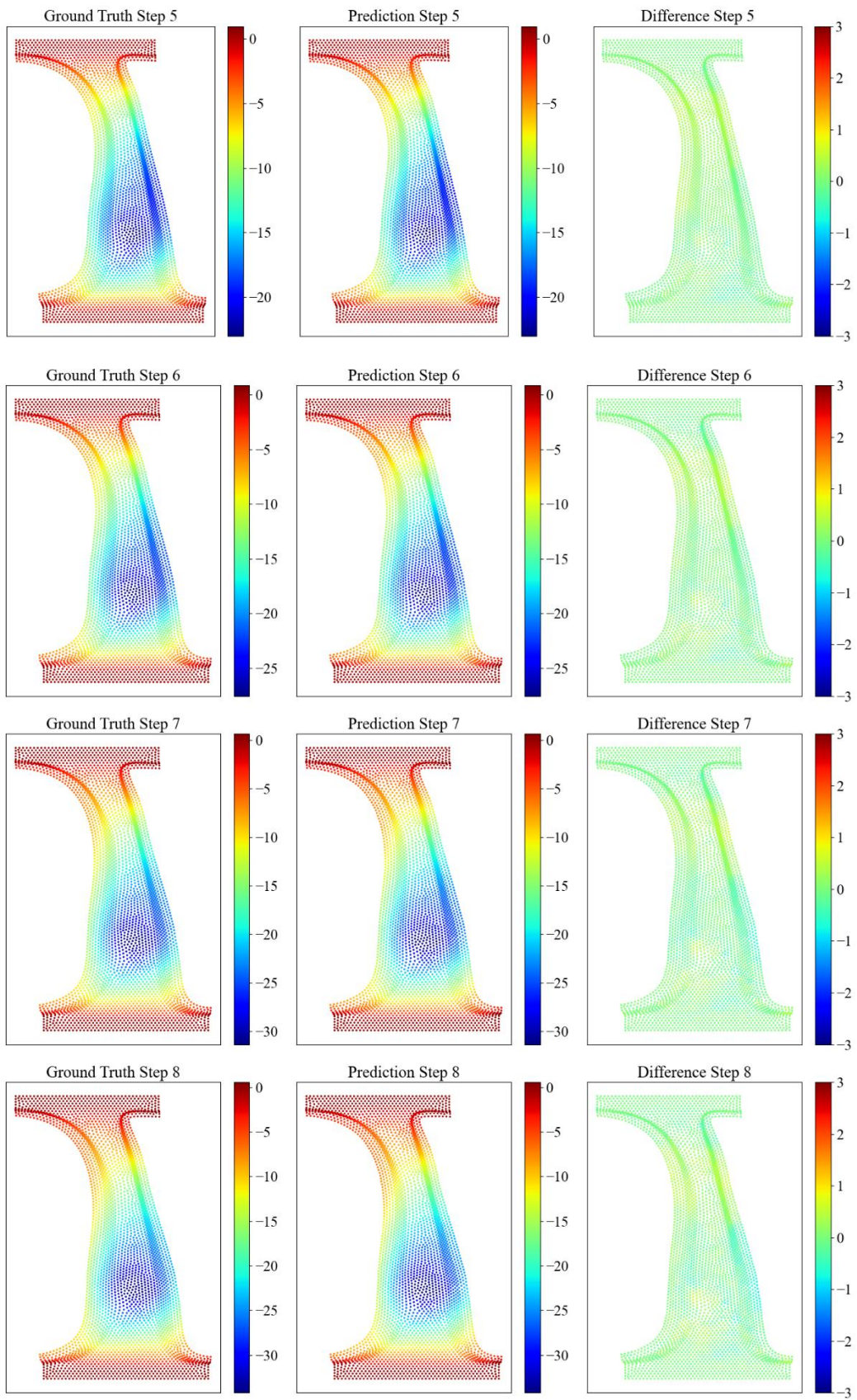
17. Liu, Q., et al., *Fluid Simulation System Based on Graph Neural Network*. arXiv preprint arXiv:2202.12619, 2022.
18. He, X., Y. Wang, and J. Li, *Flow completion network: Inferring the fluid dynamics from incomplete flow information using graph neural networks*. *Physics of Fluids*, 2022. **34**(8): p. 087114.
19. Yang, Z., et al., *AMGNET: multi-scale graph neural networks for flow field prediction*. *Connection Science*, 2022. **34**(1): p. 2500-2519.
20. Li, T., et al., *Finite Volume Graph Network (FVGN): Predicting unsteady incompressible fluid dynamics with finite volume informed neural network*. arXiv preprint arXiv:2309.10050, 2023.
21. Xue, T., S. Adriaenssens, and S. Mao, *Learning the nonlinear dynamics of mechanical metamaterials with graph networks*. *International Journal of Mechanical Sciences*, 2023. **238**: p. 107835.
22. Meyer, P.P., et al., *Graph-based metamaterials: Deep learning of structure-property relations*. *Materials & Design*, 2022. **223**: p. 111175.
23. Pfaff, T., et al., *Learning mesh-based simulation with graph networks*. arXiv preprint arXiv:2010.03409, 2020.
24. Cao, Y., et al., *Efficient Learning of Mesh-Based Physical Simulation with BSMS-GNN*. arXiv preprint arXiv:2210.02573, 2022.
25. Fortunato, M., et al., *Multiscale meshgraphnets*, in *2nd AI4Science Workshop at the 39th International Conference on Machine Learning (ICML), 2022*. 2022.
26. Ronneberger, O., P. Fischer, and T. Brox. *U-Net: Convolutional Networks for Biomedical Image Segmentation*. in *Medical Image Computing and Computer-Assisted Intervention – MICCAI 2015*. 2015. Cham: Springer International Publishing.
27. Wen, Z., et al., *Data-driven spatiotemporal modeling for structural dynamics on irregular domains by stochastic dependency neural estimation*. *Computer Methods in Applied Mechanics and Engineering*, 2023. **404**: p. 115831.
28. Lea, C., et al. *Temporal convolutional networks: A unified approach to action segmentation*. in *Computer Vision–ECCV 2016 Workshops: Amsterdam, The Netherlands, October 8-10 and 15-16, 2016, Proceedings, Part III 14*. 2016. Springer.
29. Kipf, T.N. and M. Welling, *Semi-supervised classification with graph convolutional networks*. arXiv preprint arXiv:1609.02907, 2016.
30. Sanchez-Gonzalez, A., et al., *Learning to Simulate Complex Physics with Graph Networks*, in *Proceedings of the 37th International Conference on Machine Learning*, D. Hal, III and S. Aarti, Editors. 2020, PMLR: Proceedings of Machine Learning Research. p. 8459--8468.
31. Gilmer, J., et al., *Neural Message Passing for Quantum Chemistry*, in *Proceedings of the 34th International Conference on Machine Learning*, P. Doina and T. Yee Whye, Editors. 2017, PMLR: Proceedings of Machine Learning Research. p. 1263--1272.
32. Lino, M., et al., *Simulating continuum mechanics with multi-scale graph neural networks*. arXiv preprint arXiv:2106.04900, 2021.
33. Liu, W., M. Yagoubi, and M. Schoenauer. *Multi-resolution Graph Neural Networks for PDE Approximation*. in *Artificial Neural Networks and Machine Learning – ICANN 2021*. 2021. Cham: Springer International Publishing.
34. Lino, M., et al., *Towards fast simulation of environmental fluid mechanics with multi-scale graph neural networks*. arXiv preprint arXiv:2205.02637, 2022.
35. Lino, M., et al., *Multi-scale rotation-equivariant graph neural networks for unsteady Eulerian fluid dynamics*. *Physics of Fluids*, 2022. **34**(8): p. 087110.

36. Zhang, X., J. Zhou, and Z. Feng, *B-pillar collision test method*. 2020, Aiways Automobile Shanghai Co Ltd: China.
37. Li, N., *Fundamentals of Materials Modelling for Hot Stamping of UHSS Panels with Graded Properties*. Imperial College London, 2013.

Appendix

The full dynamic prediction of a representative test sample is shown in this section. The ground truth, prediction, and difference of the z-displacement of each time step is plotted in Figure 14.





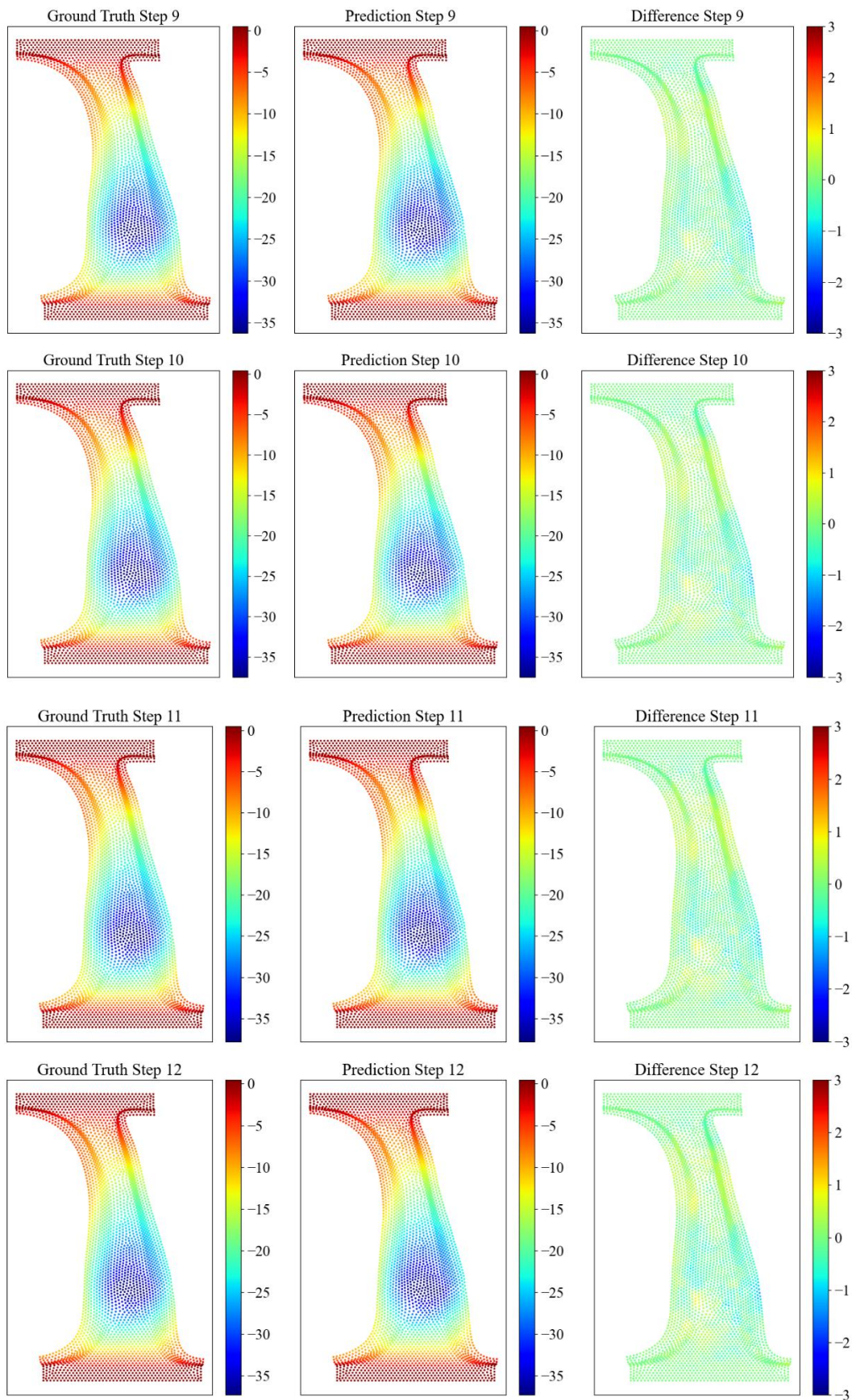


Figure 14: Full dynamic prediction of z-displacement of a test sample B-pillar.